This article has been accepted for inclusion in a future issue of this journal. Content is final as presented, with the exception of pagination.

Orthogonal Input Signal Routing for Class-C-Free GaN MMIC Doherty Power Amplifiers

Haoyang Jia, *Member, IEEE*, Ruijia Liu, *Member, IEEE*, Lin Qi, *Graduate Student Member, IEEE*, and Anding Zhu, *Fellow, IEEE*

***Abstract*—Conventional Doherty power amplifiers (DPAs) typically employ a Class-C-biased peaking amplifier to realize the delayed activation required for load modulation. The strongly nonlinear conduction behavior associated with Class-C operation introduces gain variation and intermodulation distortion, degrading the linearity performance of the DPA. This article proposes an orthogonal input signal routing (OISR) technique that decouples peaking-amplifier activation from nonlinear device biasing by implementing power-dependent activation at the RF input excitation domain. The OISR dynamically redistributes the input signal between two orthogonal excitation paths as the drive level increases, allowing both carrier and peaking amplifiers to operate under Class-AB/B bias while preserving the required Doherty load-modulation behavior. As a proof of concept, a 12-GHz OISR-based DPA is implemented using a 0.12-μm gallium nitride (GaN) high-electron-mobility transistor (HEMT) monolithic microwave integrated circuit (MMIC) process. The fabricated amplifier achieves 36.48 dBm saturated output power, 38.23% peak power-added efficiency (PAE), and 24.08% PAE at 6-dB output power back-off (PBO). Under a 100-MHz 5G NR 64-QAM signal with an 8.1-dB peak-to-average power ratio (PAPR), it achieves an adjacent channel leakage ratio (ACLR) of −43.43 dBc and an error vector magnitude (EVM) of 2.55% without digital predistortion (DPD), demonstrating high intrinsic linearity together with efficient Doherty operation.**

***Index Terms*—Class-C, Doherty, efficiency enhancement, FR3, gallium nitride (GaN), monolithic microwave integrated circuit (MMIC), linearity, power amplifier (PA).**

I. Introduction

THE increasing use of wideband, high-order modulation signals in modern wireless communication systems places stringent and often conflicting requirements on RF power amplifiers (PAs), particularly in terms of efficiency and linearity. The PA design becomes more challenging in the upper midband, including the frequency range between 7 and 24 GHz (FR3), which is being actively considered for future wireless networks due to its combination of available spectrum and favorable propagation characteristics compared with conventional millimeter-wave bands [1]. At these frequencies, monolithic microwave integrated circuit (MMIC) implementations provide an attractive solution for realizing compact and highly integrated transmitter front ends.

To maintain high efficiency under signals with large peak-to-average power ratios (PAPRs), various efficiency-enhancement architectures have been extensively investigated, including outphasing PAs, Doherty PAs (DPAs), and load-modulated balanced amplifiers (LMBAs) [2], [3], [4], [5], [6], [7], [8], [9], [10], [11], [12], [13], [14], [15], [16], [17], [18], [19]. Among these architectures, the DPA has been widely adopted because of its effective back-off efficiency enhancement and relatively low implementation complexity. The key to Doherty operation is the power-dependent activation of the peaking amplifier, which modulates the effective load impedance presented to the carrier amplifier as the input drive level increases. In a conventional DPA, this delayed activation is typically realized by biasing the peaking amplifier in Class-C operation, as illustrated in Fig. 1(a). At low input power, the peaking device remains inactive, while above the transition point its output current progressively increases to establish the desired load-modulation trajectory.

Although this approach provides a simple and effective mechanism for realizing Doherty load modulation, it intrinsically couples peaking-amplifier activation to the nonlinear conduction behavior of the active device. In particular, the small conduction angle associated with Class-C operation results in a strongly nonlinear relationship between the RF input voltage and the fundamental output current, especially around the peaking turn-on region. The resulting gain variation and harmonic generation can produce significant intermodulation distortion and contribute to the gain compression commonly observed in conventional DPAs.

Various techniques have been developed to mitigate the linearity degradation in DPAs. Digital predistortion (DPD) can effectively compensate for nonlinear distortion [20], [21], [22], but it requires additional signal processing and generally relies on observation and adaptation circuitry. Digitally driven dual-input DPAs provide additional control over the individual carrier and peaking excitation paths [23], at the expense of increased transmitter complexity. Adaptive-bias techniques

Received 15 August 2026; revised 2 October 2026; accepted 24 October 2026. This work was supported by Taighde Éireann—Research Ireland through the Research Ireland Center for Future Networks (CONNECT) under Grant 13/RC/2077_P2. *(Corresponding author: Haoyang Jia.)*

Haoyang Jia and Lin Qi are with the School of Electrical and Electronic Engineering, University College Dublin, Dublin 4, D04 V1W8 Ireland (e-mail: haoyang.jia@ucdconnect.ie; lin.qi@ucdconnect.ie).

Ruijia Liu is with the School of Electrical and Electronic Engineering, University College Dublin, Dublin 4, D04 V1W8 Ireland, and also with the Institute of Radio Frequency Engineering and Electronics (IHE), Karlsruhe Institute of Technology (KIT), 76131 Karlsruhe, Germany (e-mail: ruijia.liu@ucd.ie).

Anding Zhu was with the School of Electrical and Electronic Engineering, University College Dublin, Dublin 4, D04 V1W8, Ireland. He is now with the Department of Electronic Engineering, The Chinese University of Hong Kong, Hong Kong, SAR, China (e-mail: anding.zhu@cuhk.edu.hk).

Digital Object Identifier 10.1109/TMTT.2026.3748033

© 2026 The Authors. This work is licensed under a Creative Commons Attribution 4.0 License.
For more information, see https://creativecommons.org/licenses/by/4.0/

This article has been accepted for inclusion in a future issue of this journal. Content is final as presented, with the exception of pagination.

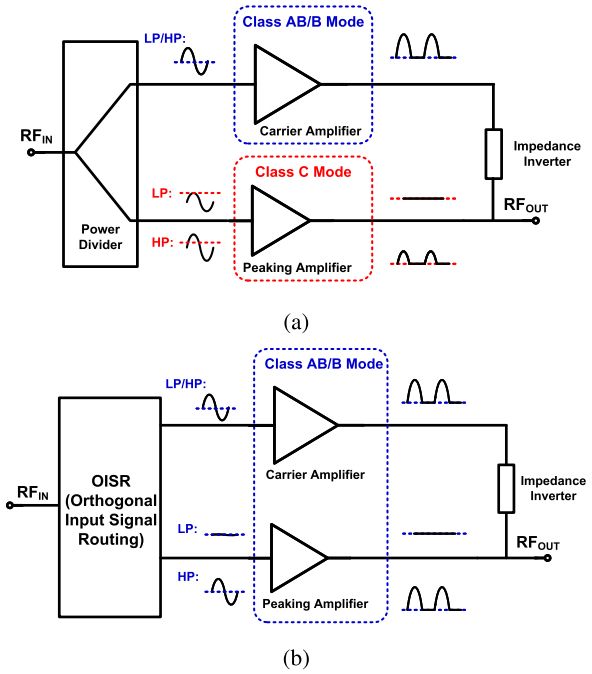


Fig. 1. (a) Conventional DPA with device-domain peaking activation. (b) Proposed OISR-DPA with excitation-domain peaking activation.

dynamically adjust the peaking-amplifier gate voltage according to the signal envelope to improve its turn-on characteristics [24], [25], [26]. Analog predistortion [27], [28], [29] and gain-compensation techniques [30], [31] have also been introduced to improve PA linearity. While these approaches can provide substantial performance improvements, they primarily compensate for or reshape the nonlinear characteristics of the PA. In single-input DPAs, the delayed activation required for load modulation generally remains tied to the bias-dependent nonlinear conduction of the peaking device.

In this work, to address this issue, an orthogonal input signal routing (OISR) technique is proposed to realize power-dependent peaking activation through RF input signal redistribution rather than Class-C biasing. As illustrated in Fig. 1(b), the OISR dynamically redistributes the input signal between two orthogonal excitation paths according to the input drive level. At low input power, the RF signal is routed only to the carrier amplifier, with the peaking amplifier remaining unexcited. As the input power exceeds the designed transition level, the OISR redirects part of the input signal to the peaking path, allowing both branches to contribute to the output power and establish the required Doherty load modulation. In this way, the delayed peaking activation is transferred from the device-bias domain to the RF-excitation domain, enabling both carrier and peaking amplifiers to operate with larger conduction angles, such as Class-AB/B, while preserving the fundamental Doherty operating mechanism.

For proof of concept, a 12-GHz OISR-based DPA is implemented in a 0.12-μm gallium nitride (GaN) high-electron-mobility transistor (HEMT) MMIC process. The fabricated amplifier achieves a saturated output power of 36.48 dBm, a peak power-added efficiency (PAE) of 38.23%

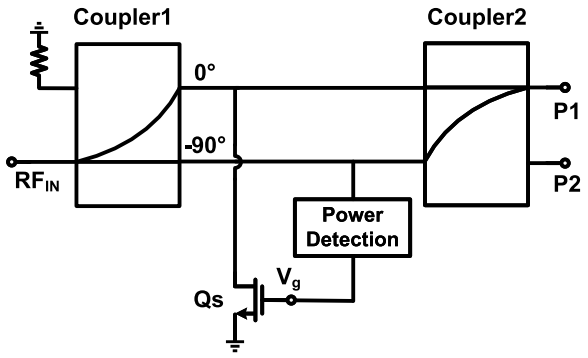


Fig. 2. Block diagram of the proposed OISR.

and 24.08% PAE at 6-dB output power back-off (PBO). Under a 100-MHz, 8.1-dB-PAPR 64-QAM 5G NR signal, the amplifier achieves an adjacent channel leakage ratio (ACLR) of −43.43 dBc and an error vector magnitude (EVM) of 2.55% without DPD. These results demonstrate that the proposed OISR provides an effective mechanism for preserving Doherty back-off efficiency while substantially improving the linearity of the DPA.

The remainder of this article is organized as follows. Section II introduces the operating principle of the proposed OISR and develops the theoretical analysis for Doherty operation. Section III investigates the practical design considerations of the OISR, including the switching device and power-detection circuit (PDC). Section IV presents the implementation of the OISR-based GaN MMIC DPA. Section V gives the experimental results, followed by the conclusion in Section VI.

II. Operating Principle of the Proposed OISR

In a conventional DPA, the delayed activation of the peaking amplifier is typically realized through Class-C biasing. Although this provides the power-dependent auxiliary current required for Doherty load modulation, the reduced conduction angle introduces a strongly nonlinear relationship between the RF input voltage and the fundamental output current, particularly around the turn-on region. The proposed OISR separates the required peaking-amplifier activation from the nonlinear conduction behavior of the active device. Instead of controlling the peaking current through Class-C biasing, OISR controls the RF excitation delivered to the peaking amplifier as a function of input drive level. Consequently, both carrier and peaking amplifiers can operate under Class-AB/B bias, while the power-dependent excitation relationship required for Doherty load modulation is established by the input routing network.

A. Architecture and Operating States of the Proposed OISR

Fig. 2 shows the block diagram of the proposed OISR. The network consists of two quadrature couplers, a transistor switch Q_s, and a PDC. Here, the term “orthogonal” refers to the nominal 90° phase relationship between the through and coupled signals generated by the quadrature couplers. The

This article has been accepted for inclusion in a future issue of this journal. Content is final as presented, with the exception of pagination.

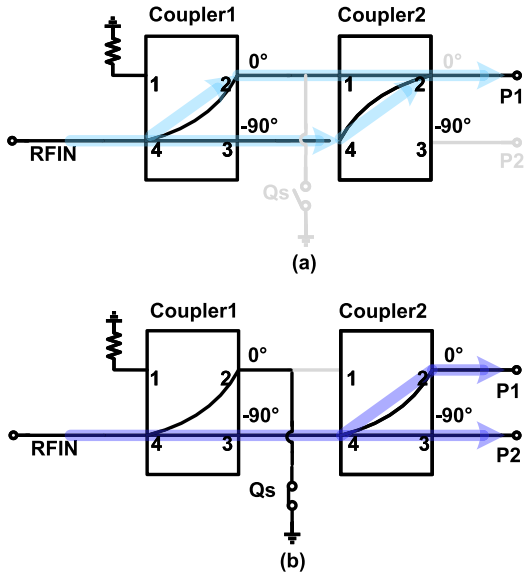


Fig. 3. Operating modes of the proposed OISR. (a) Low-power level. (b) High-power level.

two output ports, P_1 and P_2, are connected to the carrier and peaking amplifier branches, respectively.

The operating state of Q_s is controlled by the input power through the PDC. The PDC senses a fraction of the RF input signal from Coupler 1 and generates the gate-control voltage V_g for Q_s. When the input power is below the designed transition level, V_g keeps Q_s in the OFF state. As the input drive exceeds the transition level, V_g increases and turns Q_s ON, thereby changing the interference condition between the two quadrature signal paths.

The equivalent signal-routing conditions in the two operating regions are illustrated in Fig. 3. In the low-power (LP) region, as shown in Fig. 3(a), Q_s is OFF. The through and coupled signals generated by Coupler 1 propagate to Coupler 2 with the required relative phase. They combine constructively at P_1 and destructively at P_2. Ideally, therefore, the RF input signal is delivered only to P_1, while the signal at P_2 is completely suppressed. The carrier amplifier is consequently excited, whereas the peaking amplifier remains inactive despite being biased in Class-AB/B mode.

In the high-power (HP) region, Q_s is turned ON, as shown in Fig. 3(b). The coupled path of Coupler 1 is then terminated through Q_s, altering the interference condition at Coupler 2. The remaining input signal is divided between P_1 and P_2 with a nominal 90° phase difference. Both the carrier and peaking amplifiers are therefore excited. In this manner, OISR realizes the power-dependent activation of the peaking branch through RF signal routing while maintaining continuous excitation of the carrier branch.

The key distinction from a conventional DPA is therefore the physical mechanism used to generate the peaking current. In the conventional architecture, the RF excitation is continuously applied to the peaking device, and its nonlinear Class-C transfer characteristic determines when significant output current is generated. With the proposed OISR, the peaking device can instead remain biased in Class-AB/B operation, while its RF excitation is suppressed in the LP region and activated only when load modulation is required. The peaking-activation function is thus transferred from the device-bias domain to the RF-excitation domain.

B. Theoretical Analysis of OISR for Doherty Operation

To determine the signal-routing relationship required for Doherty operation, consider an OISR-based DPA in which the carrier and peaking amplifiers are driven from ports P_1 and P_2, respectively. Let d denote the normalized input drive level, with $d = 1$ corresponding to saturation and $d = \beta$ corresponding to the designed Doherty transition point. For an ideal OISR with lossless, perfectly matched couplers, the fraction of the input power routed to the peaking port can be expressed as

$$\frac{|V_2|^2}{|V_{\text{in}}|^2} = \begin{cases} 0, & 0 < d \le \beta \\ \rho_{\text{o}}, & \beta < d \le 1 \end{cases} \tag{1}$$

where V_{in} is the OISR input voltage, V_2 is the voltage delivered to the peaking branch, and ρ_o denotes the power-routing coefficient in the HP region.

According to (1), the carrier- and peaking-path excitation voltages in the HP region can be written as

$$\begin{cases} V_1 = \sqrt{(1-\rho_{\text{o}})}V_{\text{in}} \\ V_2 = \sqrt{\rho_{\text{o}}}V_{\text{in}}e^{-j90^\circ} \end{cases} \tag{2}$$

where V_1 and V_2 are the voltages delivered to the carrier and peaking amplifiers, respectively. The 90° relative phase is inherently generated by the quadrature routing network and can be incorporated into the phase relationship required by the Doherty combining network.

For proper Doherty operation, the OISR excitation profile must satisfy two conditions. First, the peaking amplifier must remain unexcited before the carrier amplifier reaches the designed break point $d = \beta$. Second, after activation, the carrier and peaking excitation levels must increase with the input drive such that their maximum output currents reach the required values simultaneously at saturation.

Let $g_{\text{m,c}}$ and $g_{\text{m,p}}$ denote the effective transconductances of the carrier and peaking devices, respectively, and let $I_{\text{M,c}}$ and $I_{\text{M,p}}$ denote their maximum fundamental output-current amplitudes. The subscripts c and p denote the carrier and peaking branches, respectively, while br and sat denote the break point and saturation. At the break point

$$\begin{cases} g_{m,\text{c}} \cdot V_{in,\text{c},br} = \dfrac{\beta \cdot I_{M,\text{c}}}{1-\cos\left(\dfrac{\theta_c}{2}\right)} \\ g_{m,\text{p}} \cdot V_{in,\text{p},br} = 0 \end{cases} \tag{3}$$

where θ_c denotes the conduction angle of the carrier amplifier. At saturation

$$\begin{cases} g_{m,\text{c}} \cdot V_{in,\text{c},sat} = \dfrac{I_{M,\text{c}}}{1-\cos\left(\dfrac{\theta_c}{2}\right)} \\ g_{m,\text{p}} \cdot V_{in,\text{p},sat} = \dfrac{I_{M,\text{p}}}{1-\cos\left(\dfrac{\theta_p}{2}\right)} \end{cases} \tag{4}$$

This article has been accepted for inclusion in a future issue of this journal. Content is final as presented, with the exception of pagination.

where θ_p denote the conduction angle of the peaking amplifier. From (4), the required voltage-excitation ratio at saturation can therefore be expressed as

$$K_V = \frac{V_{in,p,sat}}{V_{in,c,sat}} = \frac{I_{M,p}}{I_{M,c}} \cdot \frac{1-\cos\left(\frac{\theta_c}{2}\right)}{1-\cos\left(\frac{\theta_p}{2}\right)} \cdot \frac{g_{m,c}}{g_{m,p}}. \tag{5}$$

For a DPA designed with a normalized break point β, the required maximum current relationship is

$$I_{M,p} = \frac{1-\beta}{\beta} I_{M,c}. \tag{6}$$

The OISR power-routing coefficient must therefore be selected to provide the required carrier-to-peaking excitation ratio. Considering the input impedances $R_{in,c}$ and $R_{in,p}$ of the two amplifier branches

$$\rho_o = \frac{P_{in,p}}{P_{in,DPA}} = \frac{K_V^2}{\frac{R_{in,p}}{R_{in,c}} + K_V^2} \tag{7}$$

where $P_{in,DPA}$ is the input power of the overall DPA. For the symmetric case considered in this work, the carrier and peaking amplifiers employ identical output devices and are both operated close to Class-B/AB conditions. Assuming approximately equal effective transconductances, input impedances, and conduction angles for the two branches, (7)–(9) reduce to the following equation after substituting (2) and (3):

$$\rho_o = \frac{1}{1+\left(\frac{\beta}{1-\beta}\right)^2}. \tag{8}$$

Equation (8) directly relates the required OISR power-routing coefficient to the desired Doherty back-off level. For a conventional 6-dB DPA, $\beta = 0.5$, giving $\rho_o = 0.5$. Therefore, equal power division between the carrier and peaking excitation paths is required in the HP region, which can be naturally realized using 3-dB quadrature couplers.

To verify that this excitation relationship preserves the desired Doherty load modulation, the effective load impedances presented to the carrier and peaking amplifiers can be expressed, following conventional DPA theory, as:

$$Z_C = \begin{cases} \frac{Z_{opt}}{\beta}, & 0 < d \le \beta \\ \frac{Z_{opt}}{d}, & \beta < d \le 1 \end{cases} \tag{9}$$

$$Z_P = \begin{cases} \infty, & 0 < d \le \beta \\ (1-\beta) Z_{opt} \frac{d}{d-\beta}, & \beta < d \le 1 \end{cases} \tag{10}$$

where Z_C and Z_P denote the load impedances seen by the carrier and peaking devices, respectively, and Z_{opt} represents the optimum load impedance. Using the relationship between β and ρ_o established in (8), these expressions can equivalently be written in terms of the OISR routing coefficient as follows (9) and (10), giving

$$Z_C = \begin{cases} \left(1+\sqrt{\frac{\rho_o}{1-\rho_o}}\right) Z_{opt}, & 0 < d \le \beta \\ \frac{Z_{opt}}{d}, & \beta < d \le 1 \end{cases} \tag{11}$$

$$Z_P = \begin{cases} \infty, & 0 < d \le \beta \\ \frac{\sqrt{\rho_o}}{\sqrt{\rho_o}+\sqrt{1-\rho_o}} \frac{d}{d-\frac{\sqrt{1-\rho_o}}{\sqrt{\rho_o}+\sqrt{1-\rho_o}}} \cdot Z_{opt}, & \beta < d \le 1. \end{cases} \tag{12}$$

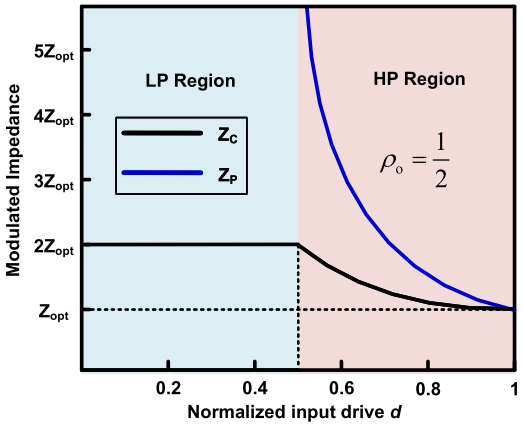


Fig. 4. Calculated modulated impedance curves using the proposed OISR in DPA.

Fig. 4 shows the calculated normalized load-modulation trajectories for the 6-dB design considered in this work. With $\rho_o = 0.5$, the carrier impedance remains at $2Z_{opt}$ in the LP region and decreases toward Z_{opt} after the peaking branch is activated. Meanwhile, the peaking impedance transitions from an open-circuit condition at the break point toward Z_{opt} at saturation. The resulting trajectories are therefore identical to those required for an ideal symmetric 6-dB DPA.

III. Design Considerations of the Proposed OISR

The theoretical analysis in Section II assumes ideal power-dependent signal routing between the carrier and peaking branches. In a practical implementation, however, the transition between the LP and HP routing states is determined by the finite impedance of the switching transistor and the response of the PDC. These nonidealities directly affect the carrier-to-peaking excitation ratio, the peaking activation point, and ultimately the load-modulation behavior of the DPA. This section therefore investigates the practical implementation of the OISR, with particular emphasis on the switching device and the PDC.

A. Effect of the Switching Device

For the 6-dB-PBO DPA, Section II shows that the required HP routing coefficient is $\rho_o = 0.5$. Therefore, 3-dB quadrature

This article has been accepted for inclusion in a future issue of this journal. Content is final as presented, with the exception of pagination.

couplers are employed in the OISR to provide equal carrier and peaking excitation at the designed HP condition.

In the ideal LP state, the switch Q_s is open, allowing the two signals generated by Coupler 1 to propagate to Coupler 2 and establish constructive interference at the carrier port and destructive interference at the peaking port. In practice, the OFF-state impedance of Q_s is finite because of device parasitics, resulting in incomplete cancellation at the peaking port. Conversely, in the HP state, Q_s presents a finite ON-state impedance rather than an ideal short circuit, which modifies the termination presented to Coupler 1 and consequently affects the power division between the carrier and peaking paths.

To illustrate the influence of the switching device, the ON-state behavior can first be represented by an equivalent resistance R_{on}. Assuming ideal, lossless 3-dB couplers with a reference impedance Z_0, the equivalent termination seen from port 3 of Coupler 1 can be written as

$$Z_{c13} = R_{on} \| Z_o. \tag{13}$$

The power components delivered from Coupler 1 to Coupler 2 are then determined by this termination. For the ideal 3-dB coupling condition, they can be expressed as

$$P_{c23} = \frac{1}{2} P_{in} \tag{14}$$

and

$$P_{c22} = \frac{1}{2} P_{in} \cdot \frac{R_{on}}{R_{on} + Z_o} \tag{15}$$

where P_{c22} and P_{c23} represent the output power at the ports 2 and 3 of Coupler 2, and P_{in} denotes the input power, given by $P_{in} = i_{in}^2 Z_o$. After recombination in Coupler 2, the carrier- and peaking-port powers are determined by the amplitude and phase relationships between these two signal components. As R_{on} changes from a high value toward its ON-state value, the interference condition gradually changes from the LP routing state, in which the peaking-port excitation is strongly suppressed, toward the HP state, in which power is delivered to both amplifier branches.

This behavior is important because the OISR does not require an instantaneous binary transition between two ideal switch states. Instead, the continuous variation of the effective switch impedance provides a smooth redistribution of RF excitation between the carrier and peaking paths around the Doherty transition point. The practical routing characteristic is therefore determined by both the nonlinear R_{on}-versus-V_g behavior of Q_s and the transfer characteristic of the PDC.

In the practical implementation, a GaN HEMT is employed as Q_s. Its device size represents a tradeoff between ON-state resistance and OFF-state parasitic capacitance. A larger device reduces the ON-state resistance and therefore provides a termination closer to the desired HP condition, but its increased parasitic capacitance degrades isolation in the LP state. Conversely, a smaller device improves the OFF-state isolation but introduces a larger ON-state resistance. The device dimensions are therefore optimized using the nonlinear transistor model together with the complete electromagnetic model of the two quadrature couplers.

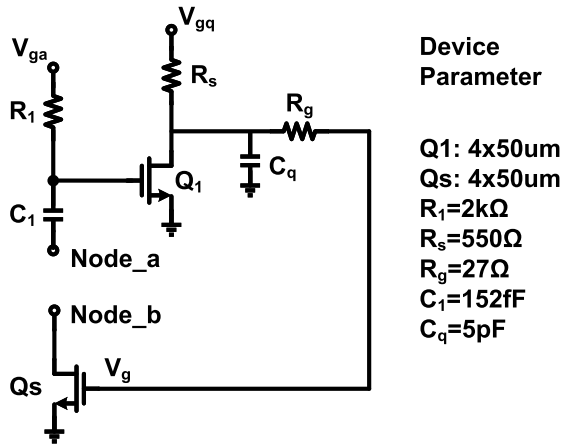


Fig. 5. Simplified circuit diagram of the designed PDC.

B. Power-Dependent Control of the OISR

To achieve adaptive power-dependent routing, the gate voltage of Q_s is controlled by the PDC shown in Fig. 5. The PDC senses a fraction of the RF input signal from the coupled port of Coupler 1 and converts the RF drive level into a control voltage V_g. As a result, the routing state of the OISR is determined directly by the instantaneous input-signal envelope without requiring an external control signal.

At low input power, the detected voltage remains below the turn-on level of Q_s. The switch therefore presents a high impedance, and the two orthogonal signal components are recombined at Coupler 2 such that the carrier-port signal is reinforced while the peaking-port signal is suppressed. Consequently, only the carrier amplifier is effectively excited in the LP region.

As the input power increases, the detected voltage rises and progressively turns on Q_s. The resulting reduction in switch impedance changes the termination condition at Coupler 1 and therefore modifies the relative signal components applied to Coupler 2. Power is progressively redirected toward the peaking port while the carrier port remains continuously excited. The peaking amplifier is thus activated around the designed Doherty transition point without changing its Class-AB/B gate bias. The auxiliary bias voltage V_{ga} in the PDC provides an additional degree of freedom for controlling the transition point. By adjusting V_{ga}, the detected voltage required to turn on Q_s can be shifted, allowing the peaking activation point to be aligned with the desired PBO level. This freedom is particularly useful in practice because the optimum transition point can be affected by device characteristics, coupler losses, and other circuit nonidealities.

Figs. 6 and 7 show the simulated control voltage and the corresponding signal-routing behavior as the input power increases. Due to the nonideal switching behavior of the PDC circuit, a finite transition region exists between the LP and HP modes. As shown in Fig. 6, a more negative V_{ga} produces a steeper variation in V_g as the proposed OISR switches from the LP mode to the HP mode. Therefore, the gate bias voltage V_{ga} is selected to provide a steep control-voltage

This article has been accepted for inclusion in a future issue of this journal. Content is final as presented, with the exception of pagination.

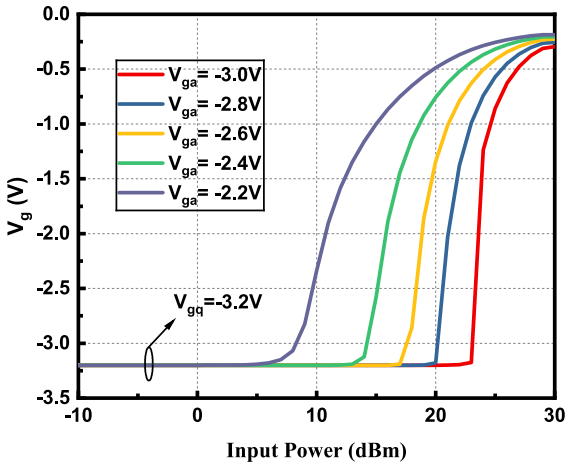


Fig. 6. Simulated V_g versus input power with different values of V_{ga}.

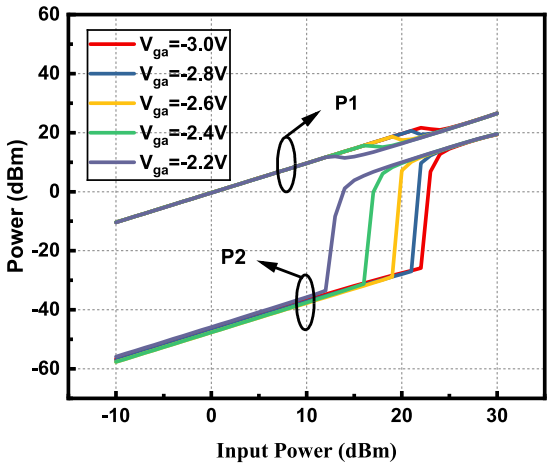


Fig. 7. Simulated power curves of the proposed OISR as power increases when $V_{gq} = -3.2$ V.

response, thereby confining this transition to a narrow input-power range. From Fig. 7, it can be seen that the peaking-path power remains strongly suppressed in the LP region, while the carrier-path power increases with the input drive. In this design, $V_{ga} = -2.6$ V provides the required 6-dB PBO range while maintaining a narrow transition region, such that the resulting power leakage and nonlinear effects remain very limited. Around the designed transition point, the control voltage rises sufficiently to turn on Q_s, causing the peaking-path power to increase rapidly. Beyond this point, both paths are excited and gradually approach the carrier-to-peaking excitation relationship required for 6-dB-PBO Doherty operation, as derived in Section II.

This simulated behavior confirms that the combination of the PDC and switching transistor converts the input-power variation into the required RF-routing characteristic. Importantly, the nonlinear transition is confined primarily to the LP control and routing network rather than being generated by low-conduction-angle operation of the HP peaking device. The peaking PA itself can therefore remain under Class-AB/B bias while its RF excitation is controlled externally by the OISR.

It is worth noting that the OISR employs two quadrature couplers and the PDC circuit to achieve power-dependent orthogonal signal routing for delayed activation. These components introduce additional insertion loss at the input stage, especially in HP mode, primarily due to power dissipation in Q_s. Since the OISR is located at the DPA input, where the RF power level is substantially lower than that at the output owing to the amplifier gain exceeding 15 dB, the power dissipated in the OISR represents only a small fraction of the RF output power. Consequently, this input-network loss is expected to have a negligible impact on the overall efficiency.

C. Bandwidth Considerations of the PDC

Because the OISR is controlled by the detected RF envelope, the dynamic response of the PDC must be sufficiently fast to follow the envelope variation in wideband modulated signals. An excessively slow detector would cause the peaking excitation to lag the input envelope, introducing additional dynamic nonlinear distortion.

For the PDC employed in this work, the dominant bandwidth can be approximated as

$$f_{\text{-3dB,PDC}} = \frac{1}{2\pi R_s \parallel R_g \left(C_q + C_{ds1}\right)} \tag{16}$$

where R_s, R_g, and C_q represent the relevant resistances and capacitor in the detector network, while C_{ds1} represents the dominant device capacitance. Here, C_q introduces a tradeoff between detector response speed and voltage ripple. A smaller C_q enables a faster response but increases the ripple in V_g, which may result in power leakage of the peaking branch in HP mode. Conversely, increasing C_q reduces the ripple in V_g at the expense of a slower detector response, thereby limiting the achievable modulation bandwidth. In this work, with $C_q = 5$ pF and the component values used in the implemented detector, the estimated PDC bandwidth exceeds 1 GHz. This bandwidth is substantially larger than the normal 5G NR modulation bandwidths, allowing the detector to follow the signal-envelope variations with limited dynamic delay. The wideband response of the PDC is therefore sufficient for demonstrating the proposed OISR under the modulated-signal conditions considered in this work. For wider modulation bandwidth requirements, C_q can be further reduced, subject to the resulting ripple and leakage constraints.

Overall, the practical OISR combines the passive quadrature-routing network, the GaN HEMT switch, and the PDC to transform input-power variation into the carrier-to-peaking excitation relationship required for Doherty load modulation. The resulting circuit preserves the fundamental operating principle established in Section II while enabling both amplifier branches to remain under Class-AB/B bias.

IV. Implementation of the Proposed DPA

The schematic of the proposed OISR-based DPA implemented using a 0.12-μm GaN HEMT MMIC process is shown

This article has been accepted for inclusion in a future issue of this journal. Content is final as presented, with the exception of pagination.

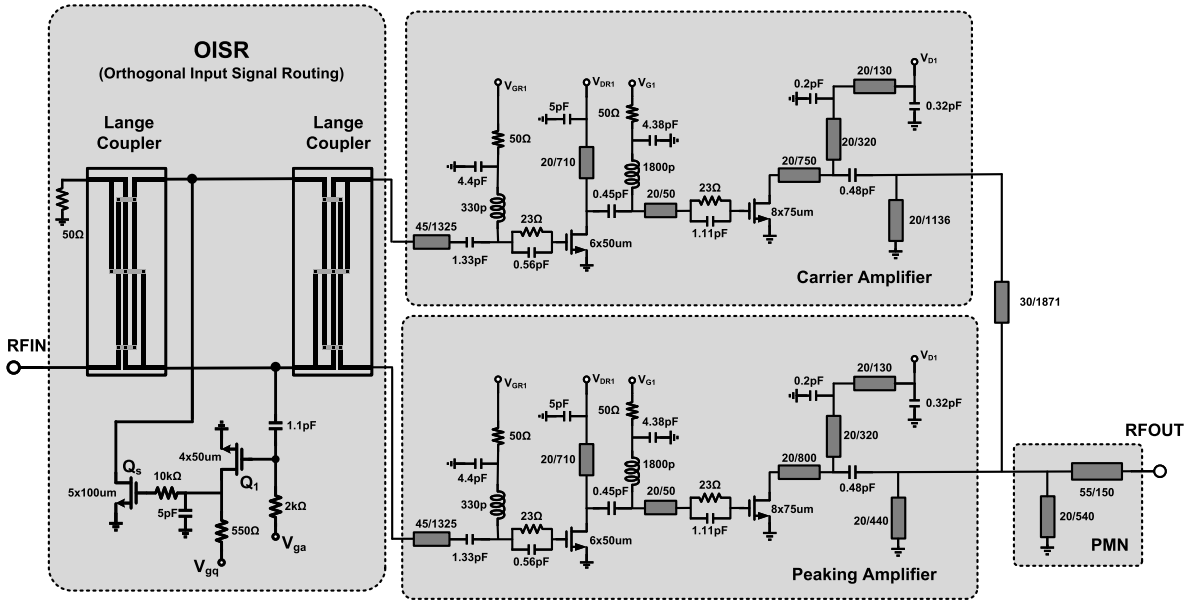


Fig. 8. Schematic of the implemented OISR-based DPA.

in Fig. 8. The OISR is integrated at the input to provide power-dependent excitation of the carrier and peaking branches. As discussed in Sections II and III, the carrier branch is continuously excited, whereas the peaking-branch excitation is suppressed in the LP region and progressively increased after the designed transition point.

The output combining network is designed to realize the load-modulation trajectory. A quarter-wavelength impedance inverter with a characteristic impedance of 60 Ω is inserted between the combining node and the peaking amplifier to establish the required impedance transformation. Since the carrier and peaking signals generated by the OISR inherently exhibit a nominal 90° phase difference, no additional input phase-compensation line is required in the peaking branch. At the output, an L-type postmatching network (PMN) transforms the 30 Ω combining-node impedance to the 50 Ω system impedance. These networks are jointly optimized with the PA cells and the OISR to account for practical MMIC losses and parasitic effects.

A. PA Design and Bias Conditions

The carrier and peaking branches employ identical two-stage PA configurations. In each branch, the output stage uses an 8×75 μm GaN HEMT to provide the required output power, while a smaller 6×50 μm device is employed in the driver stage to provide sufficient overall gain.

Unlike a conventional DPA, in which the peaking output transistor is biased in Class-C operation to obtain delayed turn-on, the output devices in both branches of the proposed DPA are biased in Class-AB operation. The delayed activation of the peaking branch is instead generated by the OISR at the input. Consequently, the peaking device remains effectively unexcited in the LP region even though its DC bias condition corresponds to Class-AB operation. Once the input drive exceeds the designed transition level, the OISR progressively routes RF power to the peaking branch, enabling its output current to contribute to the Doherty load modulation.

This distinction is important: the peaking transistor itself does not need to undergo the low-conduction-angle turn-on transition associated with conventional Class-C operation. Instead, the required power-dependent peaking current is produced by controlling its RF excitation while maintaining a substantially more linear device operating condition.

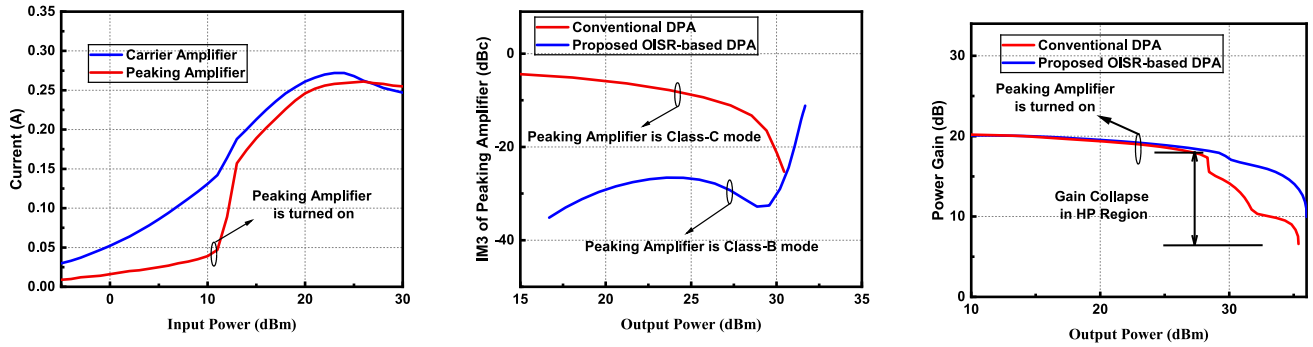
B. Simulated Operating Characteristics

To verify the operating mechanism of the proposed architecture, Fig. 9 compares the simulated carrier and peaking currents, nonlinear distortion, and gain characteristics of the OISR-based DPA with those of a conventional Class-C DPA.

Fig. 9(a) shows the simulated fundamental output currents of the carrier and peaking branches as functions of input power. In the LP region, the carrier current increases continuously with the input drive, whereas the peaking current remains close to zero because its RF excitation is suppressed by the OISR. Around the designed Doherty transition point, the peaking current begins to increase as the OISR redirects part of the input signal to the peaking branch. Both branch currents subsequently increase toward saturation, providing the current relationship required for Doherty load modulation.

Although the resulting current profile resembles that of a conventional DPA, the physical mechanism generating the peaking current is fundamentally different. In a conventional DPA, the transition is produced by the nonlinear transfer characteristic of the Class-C-biased peaking transistor. In the proposed architecture, it is produced by the power-dependent

This article has been accepted for inclusion in a future issue of this journal. Content is final as presented, with the exception of pagination.



(a) (b) (c)

Fig. 9. (a) Simulated fundamental output currents of the carrier and peaking branches. (b) Simulated IM3 of the peaking branch versus output power at 12 GHz. (c) Simulated power gain of the conventional DPA and the proposed Class-C-Free DPA.

RF-routing characteristic of the OISR, while the peaking transistor remains under Class-AB/B bias.

The linearity benefit of this approach is illustrated in Fig. 9(b), which compares the simulated third-order intermodulation (IM3) component of the peaking branch with that of a conventional Class-C implementation. The Class-C-biased peaking amplifier exhibits a pronounced increase in IM3 around its turn-on region, where the conduction angle is small, and the relationship between input voltage and fundamental output current is strongly nonlinear. In contrast, the OISR-based peaking amplifier operates under Class-AB/B bias when excited, substantially reducing the IM3 generated during peaking activation. This result directly demonstrates the principal linearity advantage of transferring the activation function from the device-bias domain to the RF-excitation domain.

The corresponding gain characteristics are shown in Fig. 9(c). The conventional DPA exhibits a noticeable gain reduction around the transition to the HP region, primarily associated with the low gain and nonlinear turn-on characteristic of the Class-C peaking amplifier. In comparison, the proposed OISR-based DPA maintains a substantially flatter gain characteristic after peaking activation. Since both PA branches operate under Class-AB/B bias, their effective RF gains are better matched, thereby reducing the gain discontinuity associated with the Doherty transition.

These simulation results demonstrate that the proposed OISR preserves the required power-dependent carrier and peaking current relationship while avoiding Class-C operation of the peaking device. The resulting reduction in peaking-branch intermodulation distortion and gain variation provides the basis for the improved linearity.

V. Measurement Results

The proposed OISR-based DPA was fabricated in a 0.12-μm GaN HEMT process. A photograph of the fabricated MMIC is shown in Fig. 10. The chip occupies an area of 2.6×3.6 mm^2. For experimental characterization, the DC pads were wire-bonded to an external test board, where decoupling capacitors were employed at the supply terminals to ensure stable bias conditions. The measurement setup is shown in Fig. 11.

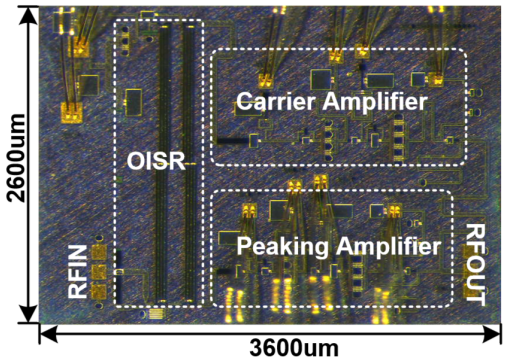


Fig. 10. Photograph of the implemented OISR-based DPA.

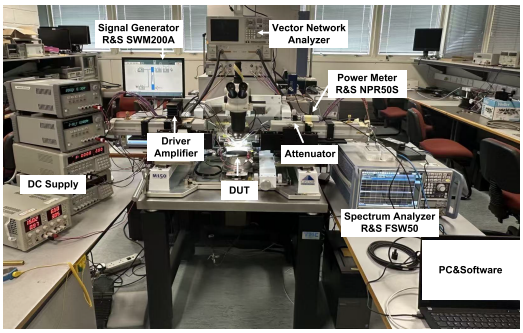


Fig. 11. Measurement setup.

During the measurements, the drain supply voltages of the driver and output stages in both the carrier and peaking branches were set to 25 V. The carrier and peaking amplifiers were biased under identical Class-AB conditions, with gate voltages of −2.08 V. Therefore, unlike a conventional DPA employing a Class-C-biased peaking device, no low-conduction-angle bias condition was used to realize delayed peaking activation.

A. Small-Signal and Continuous-Wave Performance

Fig. 12 compares the simulated and measured S-parameters of the fabricated DPA. The measured response agrees reasonably well with the simulation around the designed operating

This article has been accepted for inclusion in a future issue of this journal. Content is final as presented, with the exception of pagination.

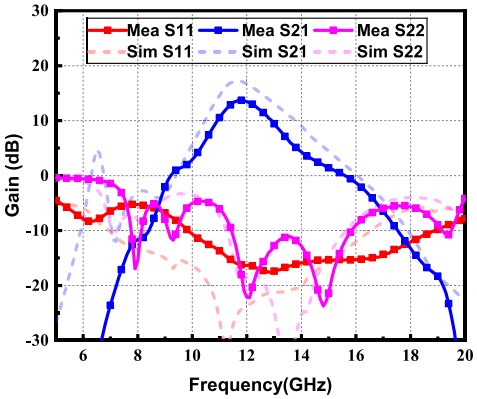


Fig. 12. Simulated and measured S-parameters.

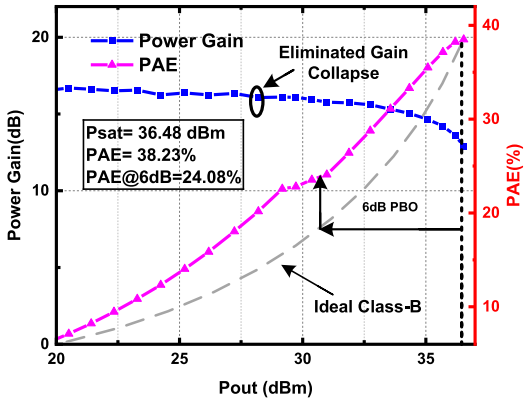


Fig. 13. Measured PAE and power gain versus output power.

frequency, confirming the functionality of the implemented input routing and amplification networks.

Fig. 13 shows the measured power gain and PAE as functions of output power at 12 GHz. The fabricated DPA achieves a saturated output power of 36.48 dBm and a peak PAE of 38.23%. At the 6-dB output PBO point, the measured PAE remains 24.08%, demonstrating the intended back-off efficiency enhancement.

More importantly, the measured gain remains relatively smooth through the Doherty transition region. In a conventional DPA, activation of the deeply Class-C-biased peaking amplifier can introduce a pronounced gain variation because of its low gain and strongly nonlinear turn-on characteristic. In the proposed architecture, the peaking amplifier is maintained under Class-AB bias, while its delayed activation is realized through the OISR. The measured gain characteristic is therefore consistent with the operating mechanism predicted by the simulations in Fig. 9, where transferring the peaking activation from the device-bias domain to the RF-excitation domain substantially reduces the gain collapse around the Doherty transition.

B. Modulated-Signal Performance

To evaluate the linearity performance of the proposed architecture, the fabricated DPA was further characterized using

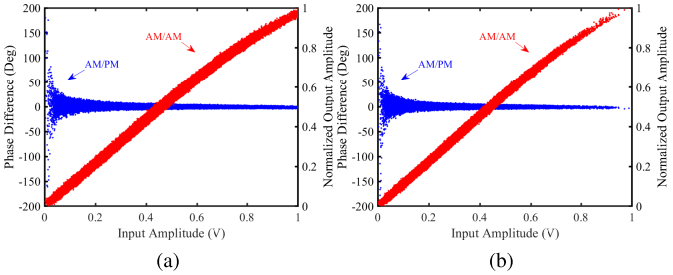


Fig. 14. AM/AM and AM/PM characteristics of the proposed DPA at 12 GHz under 100-MHz 5G NR 64-QAM excitation with (a) 6-dB PAPR and (b) 8.1-dB PAPR.

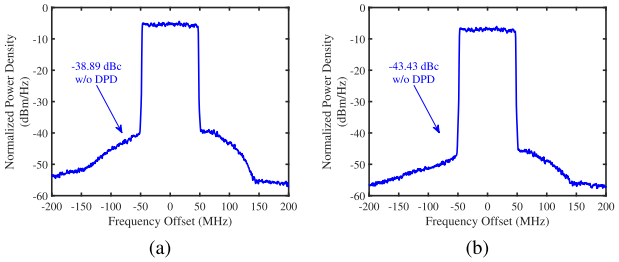


Fig. 15. Normalized output power spectral density of the proposed DPA at 12 GHz under a 100-MHz 5G NR 64-QAM signal with (a) 6-dB PAPR at 30.3-dBm average output power and (b) 8.1-dB PAPR at 28.4-dBm average output power.

100-MHz 5G NR 64-QAM modulated signals without DPD. Two signals with PAPRs of 6 and 8.1 dB were employed to investigate the nonlinear behavior under different average output-power conditions.

Fig. 14 shows the measured AM/AM and AM/PM characteristics. For both excitation conditions, the DPA exhibits a relatively smooth AM/AM response over the operating power range, with no abrupt gain discontinuity around the peaking activation region. This behavior is consistent with the OISR operating principle, in which the peaking branch is activated by gradually redistributing the RF excitation rather than by driving a Class-C device through its nonlinear turn-on region. The measured AM/PM characteristic also remains well controlled over the principal operating range.

The corresponding output spectrum is shown in Fig. 15. Under a 100-MHz modulated signal with a 6-dB PAPR, the DPA delivers an average output power of 30.3 dBm and achieves an ACLR of −38.89 dBc without DPD. For the 8.1-dB-PAPR signal, the average output power and PAE are 28.4 dBm and 22.04%, respectively, while the measured ACLR improves to −43.43 dBc, also without DPD.

The measured constellation for the 8.1-dB-PAPR signal is shown in Fig. 16. An EVM of 2.55% is obtained without DPD. Together with the measured ACLR of −43.43 dBc, this result demonstrates the excellent linearity performance of the fabricated DPA under wideband modulated excitation. Importantly, these results are obtained while maintaining the back-off efficiency enhancement associated with Doherty operation, demonstrating that high efficiency and good linearity

This article has been accepted for inclusion in a future issue of this journal. Content is final as presented, with the exception of pagination.

TABLE I
PERFORMANCE COMPARISON OF STATE-OF-THE-ART EFFICIENCY-ENHANCED PAS

Parameter	[32]MWCL'17	[33]MWCL'22	[34]TMTT'13	[35]ISSCC'26	[36]TMTT'25	[37]TMTT'26	This work
Process	0.25 μm GaN HEMT	0.10 μm GaN HEMT	0.25 μm GaN HEMT	0.15 μm GaN HEMT	0.15 μm GaN HEMT	0.12 μm GaN HEMT	0.12 μm GaN HEMT
Arch.	Doherty	Doherty	Doherty	LMBA	Doherty	Doherty	DPA
Freq. (GHz)	14.6	16.3–20.3	6.8-8.5	24.0-27.5	18/27.5	14–16	12
Gain (dB)	7	18–22	9.8	16.0-18.3	10.5/7.6	5.0–6.2	15.38
P_{sat} (dBm)	36	36.6–37.7	35	34.3-35.9	34.9/34.3	35.4-36.1	36.48
PAE_{peak}(%)	30*	23–31	38-50	28.5-33.0	30.8/22.1	25.8–30.5*	38.23
PAE_{6dB}(%)	21*	19–21	39.5-44.2*	18.1-22.8*	30.5/23.4	20.8-25.2*	24.08
Modulation	256-QAM @28MHz	64-QAM @30MHz	256-QAM @20MHz	64-QAM @400MHz	OFDM @100MHz	256-QAM @200MHz	64-QAM 100MHz
P_{avg} (dBm)	29	32.6	13.2	26.6	25	26	28.40[$]
PAE_{avg} (%)	21.13*	23	41.7	23.3	22.3/18.2	N/A	22.04[$]
ACLR[#] (dBc)	-26*	-27*	-37.0	-21.1	-29.0/-26.7	-27.6	-43.43[$]
EVM[#] (%)	N/A	N/A	N/A	19.3	N/A	8.9	2.55[$]

[@]The ratio of the gain at the saturated power to the PBO point.
[&]Gain compensation technique is applied. *Value extrapolated from graphs.
[#]Measured results without DPD. [$]Measured results with 8.1-dB PAPR signal excitation.

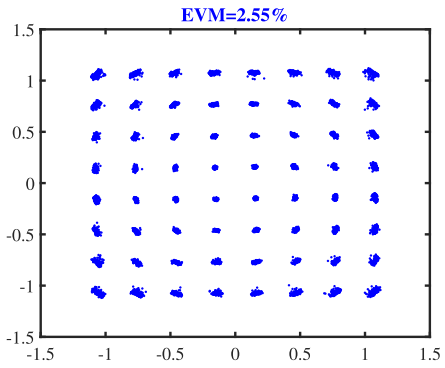


Fig. 16. Modulation constellation diagram for a 5G NR 64-QAM 100-MHz signal with 8.1-dB PAPR.

can be simultaneously achieved using the proposed excitation-domain peaking-activation mechanism.

C. Comparison With State-of-the-Art Efficiency-Enhanced PAs

Table I compares the measured performance of the proposed DPA with that of previously reported GaN efficiency-enhanced PAs, including Doherty and LMBA implementations. The fabricated OISR-based DPA achieves a saturated output power of 36.48 dBm, a peak PAE of 38.23%, and a 6-dB-back-off PAE of 24.08%. These results are competitive with the reported FR3 GaN MMIC implementations while providing a power gain of 15.38 dB.

A notable advantage of the proposed architecture is the unlinearized modulated-signal performance. Among the works listed in Table I, the proposed DPA exhibits the lowest reported ACLR of −43.43 dBc and an EVM of 2.55% without DPD. Although direct numerical comparison of linearity should be made with caution because the reported works employ different carrier frequencies, modulation formats, signal bandwidths, PAPRs, and average output-power levels, the results demonstrate that the proposed OISR can achieve strong linearity performance without sacrificing competitive output power or back-off efficiency.

These measurements experimentally validate the central concept of the proposed architecture: the delayed peaking activation required for Doherty load modulation can be implemented through power-dependent RF signal routing rather than through deeply Class-C-biased device operation. By separating the peaking-activation function from the nonlinear conduction characteristic of the power device, the proposed OISR-based DPA maintains the desired Doherty efficiency enhancement while substantially reducing the gain variation and nonlinear distortion associated with conventional peaking-amplifier turn-on.

VI. CONCLUSION

This article has presented an OISR technique for realizing Class-C-free DPAs. Unlike conventional DPAs, in which

This article has been accepted for inclusion in a future issue of this journal. Content is final as presented, with the exception of pagination.

delayed peaking activation is achieved through the nonlinear conduction characteristic of a Class-C-biased device, the proposed OISR transfers this function to the RF excitation domain. By dynamically routing the input signal between the carrier and peaking branches according to the input drive level, the required Doherty load modulation can be maintained while both amplifiers operate under Class-AB/B bias, thereby reducing the gain variation and nonlinear distortion associated with Class-C peaking activation.

A 12-GHz proof-of-concept DPA implemented in a 0.12-μm GaN HEMT MMIC process achieved a saturated output power of 36.48 dBm, a peak PAE of 38.23%, and a PAE of 24.08% at the 6-dB output PBO point. Under a 100-MHz 5G NR 64-QAM signal with an 8.1-dB PAPR, the fabricated DPA achieved an ACLR of −43.43 dBc and an EVM of 2.55% without DPD. These results demonstrate that power-dependent RF signal routing provides an effective alternative to nonlinear device biasing for peaking activation, enabling efficient Doherty operation while maintaining excellent linearity performance. More importantly, the proposed concept demonstrates that the auxiliary-path activation required in load-modulated PAs can be implemented in the excitation domain, providing a potential design approach for highly linear efficiency-enhanced RF PAs.

REFERENCES

[1] Ericsson. (2020). *6G Spectrum—Enabling the Future Mobile Life Beyond 2030*. Ericsson, White Paper. [Online]. Available: https://www.ericsson.com/en/reports-and-papers/white-papers

[2] T. W. Barton and D. J. Perreault, "Theory and implementation of RF-input outphasing power amplification," *IEEE Trans. Microw. Theory Techn.*, vol. 63, no. 12, pp. 4273–4283, Dec. 2015.

[3] T. Barton, "Not just a phase: Outphasing power amplifiers," *IEEE Microw. Mag.*, vol. 17, no. 2, pp. 18–31, Feb. 2016.

[4] R. Wu, Y.-T. Liu, J. Lopez, C. Schecht, Y. Li, and D. Y. C. Lie, "High-efficiency silicon-based envelope-tracking power amplifier design with envelope shaping for broadband wireless applications," *IEEE J. Solid-State Circuits*, vol. 48, no. 9, pp. 2030–2040, Sep. 2013.

[5] S. Hu, F. Wang, and H. Wang, "A 28-/37-/39-GHz linear Doherty power amplifier in silicon for 5G applications," *IEEE J. Solid-State Circuits*, vol. 54, no. 6, pp. 1586–1599, Jun. 2019.

[6] R. Liu, H. Jia, L. Qi, and A. Zhu, "A 24-to-30-GHz GaN MMIC Doherty power amplifier using reduced peaking intrinsic output impedance for bandwidth extension," *IEEE Microw. Wireless Technol. Lett.*, vol. 35, no. 3, pp. 362–365, Mar. 2025.

[7] I. Kim, J. Moon, S. Jee, and B. Kim, "Optimized design of a highly efficient three-stage Doherty PA using gate adaptation," *IEEE Trans. Microw. Theory Techn.*, vol. 58, no. 10, pp. 2562–2574, Oct. 2010.

[8] M. Bao, D. Gustafsson, R. Hou, Z. Ouarch, C. Chang, and K. Andersson, "A 24–28-GHz Doherty power amplifier with 4-W output power and 32% PAE at 6-dB OPBO in 150-nm GaN technology," *IEEE Microw. Wireless Compon. Lett.*, vol. 31, no. 6, pp. 752–755, Jun. 2021.

[9] E. Liu and H. Wang, "A broadband four-way parallel–series Doherty power amplifier for 5G communications," *IEEE J. Solid-State Circuits*, vol. 59, no. 5, pp. 1312–1322, May 2024.

[10] F. Wang and H. Wang, "A high-power broadband multi-primary DAT-based Doherty power amplifier for mm-Wave 5G applications," *IEEE J. Solid-State Circuits*, vol. 56, no. 6, pp. 1668–1681, Jun. 2021.

[11] R. Quaglia and S. Cripps, "A load modulated balanced amplifier for telecom applications," *IEEE Trans. Microw. Theory Techn.*, vol. 66, no. 3, pp. 1328–1338, Mar. 2018.

[12] R. Quaglia, J. Pang, S. C. Cripps, and A. Zhu, "Load-modulated balanced amplifier: From first invention to recent development," *IEEE Microw. Mag.*, vol. 23, no. 12, pp. 60–70, Dec. 2022.

[13] P. H. Pednekar, E. Berry, and T. W. Barton, "RF-input load modulated balanced amplifier with octave bandwidth," *IEEE Trans. Microw. Theory Techn.*, vol. 65, no. 12, pp. 5181–5191, Dec. 2017.

[14] P. H. Pednekar, W. Hallberg, C. Fager, and T. W. Barton, "Analysis and design of a Doherty-like RF-input load modulated balanced amplifier," *IEEE Trans. Microw. Theory Techn.*, vol. 66, no. 12, pp. 5322–5335, Dec. 2018.

[15] Y. Cao, H. Lyu, and K. Chen, "Asymmetrical load modulated balanced amplifier with continuum of modulation ratio and dual-octave bandwidth," *IEEE Trans. Microw. Theory Techn.*, vol. 69, no. 1, pp. 682–696, Jan. 2021.

[16] P. Saad and R. Hou, "Symmetrical load modulated balanced power amplifier with asymmetrical output coupling for load modulation continuum," *IEEE Trans. Microw. Theory Techn.*, vol. 70, no. 4, pp. 2315–2327, Apr. 2022.

[17] D. J. Shepphard, J. Powell, and S. C. Cripps, "A broadband reconfigurable load modulated balanced amplifier (LMBA)," in *IEEE MTT-S Int. Microw. Symp. Dig.*, Jun. 2017, pp. 947–949.

[18] Y. Cao, H. Lyu, and K. Chen, "Continuous-mode hybrid asymmetrical load- modulated balanced amplifier with three-way modulation and multi-band reconfigurability," *IEEE Trans. Circuits Syst. I, Reg. Papers*, vol. 69, no. 3, pp. 1077–1090, Mar. 2022.

[19] L. Chen, H. Liu, J. Hora, J. A. Zhang, K. S. Yeo, and X. Zhu, "A monolithically integrated single-input load-modulated balanced amplifier with enhanced efficiency at power back-off," *IEEE J. Solid-State Circuits*, vol. 56, no. 5, pp. 1553–1564, May 2021.

[20] J. Pang et al., "Broadband GaN MMIC Doherty power amplifier using continuous-mode combining for 5G sub-6 GHz applications," *IEEE J. Solid-State Circuits*, vol. 57, no. 7, pp. 2143–2154, Jul. 2022.

[21] C. Chu et al., "Waveform engineered sequential load modulated balanced amplifier with continuous class-F-1 and class-J operation," *IEEE Trans. Microw. Theory Techn.*, vol. 70, no. 2, pp. 1269–1283, Feb. 2022.

[22] P. Gong, N. B. Vangipurapu, J. Guo, and K. Chen, "Doherty-like load-modulated balanced amplifier with decade bandwidth enabled by novel broadband all-port-matched balun," *IEEE Trans. Microw. Theory Techn.*, vol. 74, no. 1, pp. 224–237, Jan. 2026.

[23] R. Darraji, F. M. Ghannouchi, and O. Hammi, "A dual-input digitally driven Doherty amplifier architecture for performance enhancement of Doherty transmitters," *IEEE Trans. Microw. Theory Techn.*, vol. 59, no. 5, pp. 1284–1293, May 2011.

[24] S. Imai, K. Mukai, H. Okabe, and T. Wada, "Dual-adaptive bias scheme of condition-tolerant Doherty power amplifier for 5G handsets," *IEEE Trans. Microw. Theory Techn.*, vol. 73, no. 5, pp. 2695–2710, May 2025.

[25] R. Liu, L. Qi, and A. Zhu, "A linearity-improved 24–29-GHz GaN MMIC Doherty power amplifier with reconfigurable self-adaptive peaking gate bias network," *IEEE Trans. Microw. Theory Techn.*, vol. 72, no. 12, pp. 6845–6856, Dec. 2024.

[26] H. T. Nguyen and H. Wang, "A coupler-based differential mm-Wave Doherty power amplifier with impedance inverting and scaling baluns," *IEEE J. Solid-State Circuits*, vol. 55, no. 5, pp. 1212–1223, May 2020.

[27] K. Yamauchi, K. Mori, M. Nakayama, Y. Mitsui, and T. Takagi, "A microwave miniaturized linearizer using a parallel diode with a bias feed resistance," *IEEE Trans. Microw. Theory Techn.*, vol. 45, no. 12, pp. 2431–2435, Dec. 1997.

[28] Z. Xiao et al., "A Ka-band CMOS power amplifier with OP1dB improvement employing a diode-connected analog linearizer," *IEEE Trans. Circuits Syst. II, Exp. Briefs*, vol. 70, no. 6, pp. 2271–2275, Jun. 2023.

[29] L. Li et al., "A linearity-enhanced millimeter-wave CMOS Doherty power amplifier using hybrid analog techniques," *IEEE Microw. Wireless Technol. Lett.*, vol. 36, no. 7, pp. 1148–1151, Jul. 2026.

[30] J. Chen et al., "A multistage GaAs HBT sequential LMBA with tailored adaptive biasing and gain coordination for linearity enhancement," *IEEE Trans. Microw. Theory Techn.*, vol. 74, no. 2, pp. 1558–1571, Feb. 2026.

[31] C. Zhao et al., "A Ka-band pseudo-Doherty load-modulated balanced amplifier with gain flatness enhancement technique," *IEEE Trans. Microw. Theory Techn.*, vol. 72, no. 6, pp. 3423–3437, Jun. 2024.

[32] R. Quaglia, V. Camarchia, J. J. M. Rubio, M. Pirola, and G. Ghione, "A 4-W Doherty power amplifier in GaN MMIC technology for 15-GHz applications," *IEEE Microw. Wireless Compon. Lett.*, vol. 27, no. 4, pp. 365–367, Apr. 2017.

[33] A. Piacibello et al., "A 5-W GaN Doherty amplifier for Ka-band satellite downlink with 4-GHz bandwidth and 17-dB NPR," *IEEE Microw. Wireless Compon. Lett.*, vol. 32, no. 8, pp. 964–967, Aug. 2022.

[34] D. Gustafsson, J. C. Cahuana, D. Kuylenstierna, I. Angelov, N. Rorsman, and C. Fager, "A wideband and compact GaN MMIC Doherty amplifier for microwave link applications," *IEEE Trans. Microw. Theory Techn.*, vol. 61, no. 2, pp. 922–930, Feb. 2013.

This article has been accepted for inclusion in a future issue of this journal. Content is final as presented, with the exception of pagination.

[35] L. Yu et al., "20.5 A 24-to-27.5GHz self-adaptive load-modulated balanced amplifier for integrated communication, sensing, and power transfer scenarios," in *IEEE Int. Solid-State Circuits Conf. (ISSCC) Dig. Tech. Papers*, Feb. 2026, pp. 348–350.
[36] Y. Tang, W. Feng, D. Zeng, and W. Che, "A K/Ka dual-band GaN MMIC Doherty power amplifier using dual out-of-phase current combining," *IEEE Trans. Microw. Theory Techn.*, vol. 73, no. 12, pp. 10384–10396, Dec. 2025.
[37] R. Liu, H. Jia, Q. Wu, J. Xia, and A. Zhu, "A hybrid-biased dual-band GaN MMIC Doherty power amplifier for 6G FR3," *IEEE Trans. Microw. Theory Techn.*, vol. 74, no. 2, pp. 1507–1517, Feb. 2026.



Haoyang Jia (Member, IEEE) received the B.E. and M.E. degrees from South China University of Technology (SCUT), Guangzhou, China, in 2019 and 2022, respectively. He is currently pursuing the Ph.D. degree at the RF and Microwave Research Group, University College Dublin (UCD), Dublin, Ireland.

His current research interests include integrated high-efficiency power amplifier (PA) design and next-generation transmitter/receiver design.

Dr. Jia was a recipient of the 2025 IEEE MTT-S Graduate Fellowship Award.



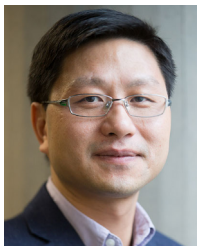
Ruijia Liu (Member, IEEE) received the B.E. degree in electronic information science and technology from Southwest Jiaotong University, Chengdu, China, in 2017, and the Ph.D. degree in electromagnetic field and microwave technology from Southeast University, Nanjing, China, in 2022.

From October 2022 to August 2024, he was a Post-Doctoral Research Fellow with the RF and Microwave Research Group, University College Dublin (UCD), Dublin, Ireland. He is currently a tenure-track Assistant Professor (Ad Astra Fellow) with the School of Electrical and Electronic Engineering, UCD. Since June 2026, he has also been a Humboldt Research Fellow with the Institute of Radio Frequency Engineering and Electronics (IHE), Karlsruhe Institute of Technology (KIT), Karlsruhe, Germany. His research interests include advanced GaN MMIC power amplifier and RFIC design for RF, microwave, and millimeter-wave applications.



Lin Qi (Graduate Student Member, IEEE) received the B.E. degree from Nanjing University of Science and Technology, Nanjing, China, in 2020, and the M.E. degree from Southeast University (SEU), Nanjing, in 2023. She is currently pursuing the Ph.D. degree at the RF and Microwave Research Group, University College Dublin (UCD), Dublin, Ireland.

Her current research interests include behavioral modeling and linearization for RF power amplifiers.



Anding Zhu (Fellow, IEEE) received the Ph.D. degree in electronic engineering from the University College Dublin (UCD), Dublin, Ireland, in 2004.

He is currently a Professor at the Department of Electronic Engineering, The Chinese University of Hong Kong (CUHK), Hong Kong. Before joining CUHK in August 2026, he was a Full Professor at the School of Electrical and Electronic Engineering, UCD, where he led the RF and Microwave Research Group. His research interests include high-frequency nonlinear system modeling and device characterization techniques, high-efficiency power amplifier design, wireless transmitter architectures, digital signal processing, and nonlinear system identification algorithms.

Prof. Zhu is an Elected Member of the IEEE Microwave Theory and Technology Society (MTT-S) Administrative Committee (AdCom) and currently serves as the President of IEEE MTT-S. He was a recipient of the 2021 IEEE MTT-S Microwave Prize. He served as a Track Editor of IEEE TRANSACTIONS ON MICROWAVE THEORY AND TECHNIQUES from 2020 to 2022 and is currently an Associate Editor of *IEEE Microwave Magazine*.